Dynamics and control of gold-encapped gallium arsenide nanowires imaged by 4D electron microscopy

Bin Chen[a,1], Xuewen Fu[a], Jau Tang[a,1], Mykhaylo Lysevych[b], Hark Hoe Tan[c], Chennupati Jagadish[c], and Ahmed H. Zewail[a,2]

[a]Physical Biology Center for Ultrafast Science and Technology, Arthur Amos Noyes Laboratory of Chemical Physics, California Institute of Technology, Pasadena, CA 91125; [b]Australian National Fabrication Facility, Research School of Physics and Engineering, The Australian National University, Canberra, ACT 2601, Australia; and [c]Department of Electronic Materials Engineering, Research School of Physics and Engineering, The Australian National University, Canberra, ACT 2601, Australia

Edited by Charles M. Lieber, Harvard University, Cambridge, MA, and approved October 26, 2017 (received for review May 26, 2017)

Eutectic-related reaction is a special chemical/physical reaction involving multiple phases, solid and liquid. Visualization of a phase reaction of composite nanomaterials with high spatial and temporal resolution provides a key understanding of alloy growth with important industrial applications. However, it has been a rather challenging task. Here, we report the direct imaging and control of the phase reaction dynamics of a single, as-grown free-standing gallium arsenide nanowire encapped with a gold nanoparticle, free from environmental confinement or disturbance, using four-dimensional (4D) electron microscopy. The nondestructive preparation of as-grown free-standing nanowires without supporting films allows us to study their anisotropic properties in their native environment with better statistical character. A laser heating pulse initiates the eutectic-related reaction at a temperature much lower than the melting points of the composite materials, followed by a precisely time-delayed electron pulse to visualize the irreversible transient states of nucleation, growth, and solidification of the complex. Combined with theoretical modeling, useful thermodynamic parameters of the newly formed alloy phases and their crystal structures could be determined. This technique of dynamical control aided by 4D imaging of phase reaction processes on the nanometer-ultrafast time scale opens new venues for engineering various reactions in a wide variety of other systems.

phase reaction | Au/GaAs nanowires | structural dynamics | eutectic dynamics | 4D electron microscopy

A eutectic system refers to a unique thermodynamic entity that forms a lattice structure with a specific atomic ratio between the constituents. The eutectic temperature describes the lowest temperature at which the mixed substances become fully molten. Comprehensive understanding of eutectic-related behavior offers a great potential for a wide variety of applications, including alloys for structural components and eutectic soldering in airplanes and cars (1), functional electronics in solar energy harvesting (2, 3), and eutectic bonding in chips for integrated circuits (4). Fundamental properties of solid microstructures from various eutectic reactions in complex systems depend on several factors—for example, the temperature that governs each phase reaction/transformation and interfacial nucleation of solid solutions (5, 6).

Eutectic-related phenomena have usually been studied via postprocessing measurements and were recently visualized by in situ techniques to investigate long time diffusion processes (7–13). Elucidation of the chemical/physical mechanism underlying those eutectic-related processes requires time-resolved measurements of the dynamic phase formation. However, probing eutectic-related phase reactions in nanostructures is very difficult because of the small sizes and the very short time scales involved, as well as the sensitivity issues to detect those transient processes that occur in far-from-equilibrium conditions for nanomaterials in a small quantity.

Recent development of 4D electron microscopy (4D EM) offers direct visualization of the transient behavior of individual nanostructures with high spatiotemporal resolution (14–19). Here, we report the direct observation and control of the irreversible phase reaction dynamics in free-standing Au/GaAs nanowires (NWs) by 4D EM with nanometer–nanosecond spatiotemporal resolution (Fig. 1). GaAs NWs were chosen because III–V materials possess unique properties, such as direct bandgap, high carrier mobility, the possibility of bandstructure engineering using compositional tuning, and hybrid of heterostructures, which demonstrate great potential for applications in optoelectronic and electronic devices (e.g., solar cells, sensors, and transistors) (3, 20). It is fundamentally important to investigate how these materials behave in harsh environments (e.g., laser pulse bombardment for simulating the radiation effect) for understanding their stability. Furthermore, since eutectic-related phenomena have been extensively studied in binary systems (e.g., Au–Si) under equilibrium conditions (7, 10, 11), the choice of a ternary system (Au–Ga–As) with pulsed laser excitation in 4D EM offers a window of opportunity for understanding eutectic dynamics in complex systems under nonequilibrium environment.

Significance

Imaging chemical/physical reaction dynamics at nanoscale interfaces of a composite nanostructure requires resolutions in both space and time. Using single-pulse methodology, we directly and visually capture the irreversible eutectic-related phase reactions of a single, same metal/semiconductor nanowire at nanometer–nanosecond spatiotemporal resolution by 4D electron microscopy. With a nondestructive free-standing sample preparation free from environmental disturbance that is important for statistical investigation, we have both qualitatively and quantitatively elucidated the transient phase reactions and obtained important physical properties of the newly formed phases, such as latent heat and specific heat. Our work provides an efficient way of quantitatively determining physical properties of a nanoscale object with a tiny small quantity, especially when not available in bulk counterparts.

Author contributions: B.C. and A.H.Z. designed research; B.C., X.F., and M.L. performed research; B.C., J.T., and A.H.Z. contributed new reagents/analytic tools; B.C., X.F., J.T., M.L., H.H.T., C.J., and A.H.Z. analyzed data; and B.C., X.F., J.T., M.L., H.H.T., C.J., and A.H.Z. wrote the paper.

The authors declare no conflict of interest.

This article is a PNAS Direct Submission.

[1]To whom correspondence may be addressed. Email: bchen5@caltech.edu or jautang@caltech.edu.

[2]Deceased August 2, 2016.

This article contains supporting information online at www.pnas.org/lookup/suppl/doi:10.1073/pnas.1708761114/-/DCSupplemental.

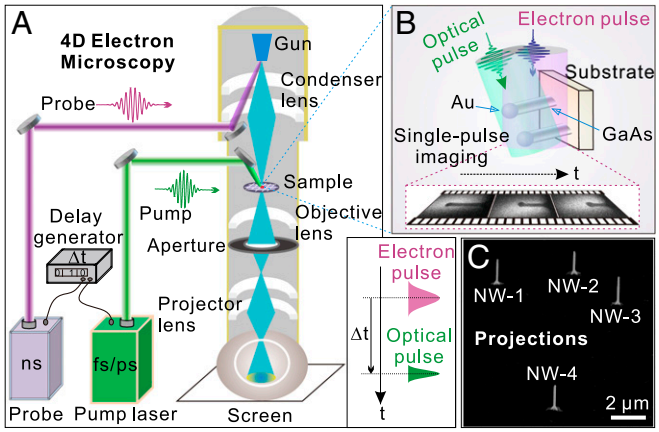

Fig. 1. The 4D EM for imaging phase reactions in a free-standing NW. (*A*) Green optical pulse enables the eutectic-related reaction of Au/GaAs NWs to be probed by a delayed electron pulse (generated by a nanosecond UV laser pulse) at a given time delay. (*B*) Scheme of free-standing NWs on substrate integrated in 4D EM (*SI Appendix*, Fig. S1). The laser heating pulse is incident upon the NW at a nearly vertical angle, while a series of eutectic-related events are captured by single-pulse methodology. (*C*) Projections of the NWs. The NWs were intentionally grown far apart from each other to exclude mutual perturbation during the measurement.

The eutectic-related phase reaction processes of the NWs are induced and controlled by a temperature jump triggered by a laser heating pulse, followed by a delayed photogenerated electron packet to probe the spatiotemporal evolution of the nanostructures. Using single-pulse imaging, one can observe the transient intermediates of the NW during the reactions. Although the raised temperatures are below the melting points for the Au bead and the underneath GaAs NW, the observed reduction in NW length and the growth of the bead size are a result of the phase reactions between the two. For the time scale, the transient nucleation and growth of the formed phases are complete within ~80 ns, while the morphological changes of the top bead last until 100 ns. The observed huge reduction rate of the NW length, which is not a simple diffusion-dominated process, will be discussed. Based on quantitative analysis and theoretical modeling of these measurements, we are able to extract useful thermodynamic parameters of the newly formed alloy phases determined by Bragg diffraction studies, leading to a better understanding of nanoscale phase reactions.

Results and Discussion

Experimental Implementation. The difficulty of unambiguously exploring the eutectic-related dynamics of a single Au/GaAs NW lies in isolating the NW from any transmission EM (TEM) supporting films (e.g., carbon films), while achieving a controllable NW geometry that is accurate enough for data analysis. We overcame this difficulty with a scheme of detecting the NWs that were grown perpendicular to the substrate surface. Namely, by directly putting the as-grown NWs still intact on the GaAs substrate (*Materials and Methods* and *SI Appendix*, Fig. S1) into the 4D EM (Fig. 1 *A* and *B*), one could exclude any sample contamination or possible ambiguity caused by the holding films usually present for normal TEM grids. This type of sample preparation is simple and nondestructive with the freedom of investigating orientation-dependent (anisotropic) properties of the samples in their native environment. Because NWs grown on a substrate have similar orientations, better statistics are achievable through choosing a number of NWs for investigation. In addition, it becomes simple for quantitative elucidation of the phenomena without a need to take into account the effect from any supporting films (e.g., heat transfer and dissipation from the films).

The GaAs substrate was carefully aligned to be parallel to the electron beam so that the free-standing NWs were visible (otherwise, a very slight misalignment or tilting of the substrate, e.g., only 0.5°, would block the electron beam for the probing of NWs, since the NWs were only hundreds of nanometers long in the direction vertical to the substrate surface). To facilitate imaging reaction dynamics from a single NW, the NWs were purposely grown on the substrate with large separation (several micrometers away from each other), as shown in the projections of the NWs (Fig. 1*C*). With this large separation among the NWs, the disturbance from any neighboring NW could be effectively avoided during the experiments. The transient morphological changes of the NWs during the eutectic-related reactions were captured by single-pulse imaging mode of 4D EM (*Materials and Methods*).

Morphology and Structure of the NW. Fig. 2 shows the typical micrographs and diffraction patterns of the Au/GaAs NWs in stroboscopic mode without the incident pump laser, in contrast to the images taken in single-pulse mode in the following sections (Figs. 3 and 4). In the images, the NWs are aligned vertically with respect to the GaAs substrate. A gold nanoparticle is located at the tip of each GaAs NW. The targeted NW has a diameter of 108 nm, and its diffraction pattern (SA-1 region) is presented in Fig. 2, *Top Right*. The pattern indicates that GaAs has a hexagonal wurtzite (WZ) structure with the growth direction oriented along the [000$\bar{1}$] direction. Shown in Fig. 2, *Middle Left*, *Inset* is a

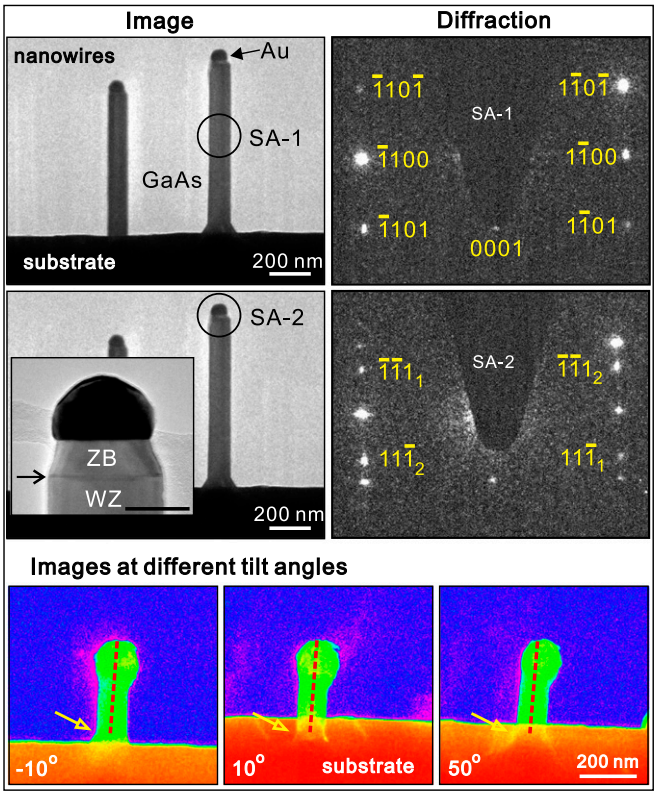

Fig. 2. Images and diffraction patterns of the Au/GaAs NWs. (*Top*) Stroboscopic image of the NW and its diffraction pattern (marked circle in the image). The diffraction pattern indicates a hexagonal WZ structure of GaAs. (*Middle*) Image and diffraction pattern of the tip region. Additional diffraction spots appeared besides the same ones as that in *Top*. These extra spots are from the cubic ZB segments, which can be seen from an enlarged image in *Middle Left*, *Inset*. (Scale bar, 50 nm.) (*Bottom*) Images of the NW at different tilting angles ranging from −10° to 50°. The dotted lines indicate the length measured from the tip to the reference point (marked by an arrow). At all angles, the NW is straight, suggesting that neither inclination nor breakage of the NW occurred after the laser pulse excitation.

typical microstructure of the NW tip. The diffraction pattern of the tip, corresponding to the SA-2 region, exhibits additional diffraction spots. The unmarked spots are the same as that in the upper diffraction pattern, which come from the WZ GaAs. The marked extra <111> ones are from the cubic zinc-blende (ZB) segments of GaAs (21). This double-spot pattern indicates a twinned ZB component. The small ZB constriction (the dark line marked by an arrow in Fig. 2, *Middle Left*, *Inset* is the ZB/WZ interface) is due to the growth termination procedure (20).

We performed further experiments in tilting conditions to verify how the NWs behaved during laser excitation (Fig. 2, *Bottom*). It demonstrated that the NWs were straight (without bending) when viewed at different tilting angles. No breakage of the NW was observed either. This experiment ensured unambiguous determination of the shrinkage of the NW length after each single-pulse laser excitation.

Imaging of Eutectic-Related Phase Reactions. To reveal the irreversible phase reactions, single-pulse imaging methodology was used. The results of the size changes of the NW are shown in Fig. 3. To obtain a clear comparison of the NW at different excitation stages, for each experiment, we enhanced the contrast between the top bead and the GaAs NW by taking two reference images with exposure to 100 electron pulses (*SI Appendix*, Fig. S2). By comparing the single-pulse images with the corresponding reference images, the length of the NW at each stage could be determined with the guide of a ruler. Initially, the GaAs NW (without the top bead) had a length of 822 nm (0 laser shot). After a laser pulse at a fluence of 5.5 mJ/cm^2, the length of the NW became 797 nm, corresponding to a ~3% shrinkage. Compared with the initial GaAs NW, there was a 40% length reduction after 23 laser pulses. The GaAs NW length (after 46 laser pulses) was finally reduced to 235 nm after the entire run

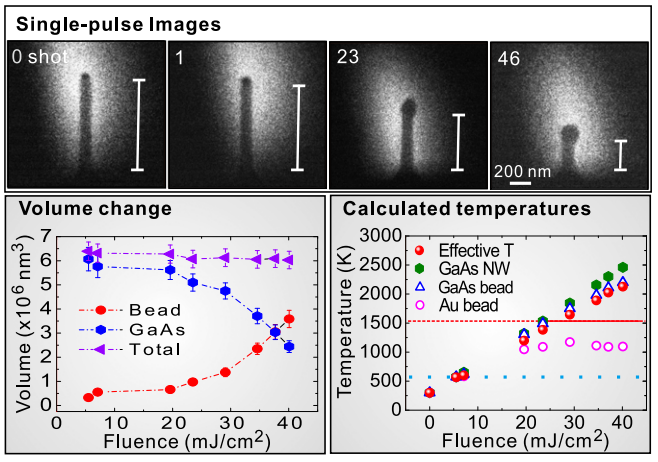

Fig. 3. Single-pulse imaging of transient changes of the NW and the calculated temperatures. (*Upper*) Single-pulse imaging of the NW length reduction due to eutectic-related reactions. The NW shrank along its axial direction, while its lateral width had no obvious change. Approximately 70% length reduction of the NW (without the top bead) was observed after a total of 46 laser shots. The rulers (white lines) indicate the NW length. The electric field polarization of the laser pulse was parallel to the long axis of the NW. (*Lower Left*) Volume change of the NW. The volume of GaAs NW reduces, while that of top bead increases. The total volume slightly decreases. (*Lower Right*) Calculated temperatures at different laser fluences. The temperature of Au or GaAs bead was estimated by assuming 100% of the component, while the effective temperature of the bead was calculated by considering the Au:GaAs ratio in the bead. The dotted line represents the lowest temperature to trigger the reaction. Because of the large latent heat of GaAs, the GaAs NW has not melted, although the temperatures (without taking account of the latent heat) are higher than its melting point (dashed line) at high fluences. The solid red line indicates the actual temperature of the GaAs NW when its latent heat is considered.

of the experiment, which was associated with a total length shrinkage of ~70%. During the whole sequence of laser heating experiments, the choice of the number of pulses and laser fluence (from 5.5 to 40 mJ/cm^2) was set so that the NW could continue its shrinkage.

Although the NW axial length decreased significantly (Fig. 3, *Upper*), no obvious width change of the NW was observed (*SI Appendix*, Fig. S3). Only the top bead—namely, the region with darker contrast than the pure GaAs part in the images—increased in size. Further analysis on the NW volume change revealed that the reduction of GaAs volume resulted in the increase of bead volume (see *SI Appendix*, Fig. S4 for the calculations). These results indicate that the GaAs body remained solid phase, while the vanished portion of the GaAs reacted with the top bead to form new phases during laser excitation.

Identification of the Phase Formation. Selected-area diffraction studies disclosed the nature of the newly formed phases during the reactions. We performed the electron diffraction in three modes: TEM (high electron counts), stroboscopic (1 kHz), and single-pulse modes (*SI Appendix*, Fig. S5 and the associated discussion). For clearly demonstrating the diffraction spots, exposure times of 5 s in TEM mode and 120 s in stroboscopic mode were chosen. For diffraction in single-pulse mode (electron pulse duration of 10 ns), the extremely low electron dose (approximately five orders of magnitude lower than that in the stroboscopic mode with an exposure time of 120 s) made it inaccessible for disclosing the irreversible transient diffraction patterns of the newly formed phases with small quantity at the nanometer–nanosecond spatiotemporal resolution. Therefore, the structures of the alloy phases were identified in the TEM mode (*SI Appendix*, Fig. S6 and Table S1).

Compared with the initial components (Fig. 2), additional diffraction spots from Au_7Ga_2 and AuGa phases appeared after the first few laser shots. According to the Au–Ga phase diagram (*SI Appendix*, Fig. S7), the temperature for Au_7Ga_2 phase (22) was much lower than the melting point of either Au (1,337 K) or GaAs (1,511 K). As more GaAs was incorporated into the top bead, eutectic phases of AuGa and $AuGa_2$ were formed. The temperature needed for this eutectic reaction, liquid $\rightarrow$ AuGa + $AuGa_2$, was 725 K, still much lower than the melting points of the individual components in the initial materials (1,337 K for Au and 1,511 K for GaAs). It is noteworthy that we only detected Au–Ga-related phases, despite the possible existence of Au–Ga–As complex according to their ternary phase diagram (23, 24). Our observations indicated that, in comparison with the Au-As complex, it was more favorable for the Au–Ga alloy formation during the nonequilibrium reaction processes. The solubility of As in Au is low, and the As species may vaporize or be removed from the interface during laser heating (25–28). The removal of the As species would lead to the slight reduction of the total volume, which was confirmed by the experimental observation in Fig. 3. We also note from *SI Appendix*, Fig. S6 that new cubic ZB segments appeared after laser pulse excitation. The length of the ZB segments was estimated to be tens of nanometers by electron diffractions at different locations of the NW with a small aperture. This result indicates that with an incoming laser pulse, the initial ZB component (Fig. 2) was alloyed with the top nanoparticle, and after laser excitation, a small amount of new ZB segments appeared again. It suggests that, compared with hexagonal WZ components, cubic ZB (normal bulk structure of GaAs) segments are preferable to precipitate near the interfacial region during nonequilibrium processes.

Calculations using the two-temperature model for Au and three-temperature model for GaAs showed that the lattice temperatures (at a fluence of 5.5 mJ/cm^2) of the top bead and GaAs body were 566 and 574 K (*SI Appendix*, Fig. S8 and Table S2), respectively, which triggered the reaction to form Au_7Ga_2 phase. At higher fluences—for example, 19.5 mJ/cm^2—the effective temperature of the top bead was 1,196 K, high enough to

facilitate the eutectic reactions for the formation of AuGa and $AuGa_2$ phases. These simulated results were in reasonably good agreement with our experimental observations.

Thermal Properties of the Newly Formed Phases. Theoretical modeling was employed to calculate the absorbed heat for both the bead and the NW so that the thermal properties for alloy phases during eutectic-related reactions could be determined (*SI Appendix*). Useful parameters, such as the latent heat and specific heat for the newly formed phases, were retrieved, and the results are summarized in Table 1. We found that the latent heats of Au_7Ga_2 and AuGa were 8 and 21 kJ/mol, while their specific heats were 62 and 41 J/(mol·K), respectively. In comparison, for the initial phases Au and GaAs, the latent heats were 12 and 106 kJ/mol, and the specific heats were 25 and 48 J/(mol·K), respectively (29, 30). The specific heat of the AuGa phase, extracted from the combination of our experimental observations with the theoretical modeling, was in reasonable agreement with the specific heat data available in the literature (31). Because of the presence of latent heat and the lower resultant bead temperature due to increasingly bigger bead size, one needed to increase laser fluences to shrink the NW further. Moreover, it was noteworthy that at high fluences (23 mJ/cm^2 or above), the GaAs NW had not melted, even though the calculated temperatures (without taking into account the latent heat for melting) were higher than its melting point (Fig. 3). This was because the energy from a laser pulse was not sufficient to overcome the large latent heat of GaAs for its melting.

Time-Resolved Dynamics. To reveal the eutectic-related dynamics, two sets of time-resolved experiments were performed on the NWs. By using a stroboscopic approach (Fig. 4, *Upper*), the integrated diffraction intensity at a low fluence of 3 mJ/cm^2 was plotted as a function of time for the time constant determination of the nonequilibrium thermodynamics of the NW. As a result of the temperature jump initiated by the heating laser pulses, the integrated diffraction intensity showed a quick decrease after time zero and then a relatively slow recovery of the diffraction intensity. The cooling time constant τ was estimated to be 123 ± 12 ns from the fitting. Aided by the extracted time scale, single-pulse imaging at that range was employed to capture the eutectic-related process of the NWs (Fig. 4, *Lower*). Three rows of the single-pulse images display the NW transient states after a single optical pulse (laser fluence of 19.5 mJ/cm^2) at different delay times. Fig. 4, *Lower Left*, *Center*, and *Right* were taken at the stages of before, at specific delays (20–100 ns), and after the process ended, respectively. It is noticed from the first row of images in Fig. 4, *Lower* that, besides a length shrinkage between the left (before) and middle (at 20 ns delay) images, a clear shape change of the top bead was observed (marked with a circle). The shape of the bead continued its change even after the incident laser pulse was removed (right image). When the delay time was 80 ns (Fig. 4, *Lower*, second row), similar behavior—namely, the length shrinkage as well as the shape change—was also seen. However, the length and shape of the NW almost remained unchanged (Fig. 4, *Lower*, third row) when observed at a delay time of 100 ns (middle) and at a state after the process ended (right). This observation indicated that the thermal energy induced by the laser heating pulse was insufficient to induce further obvious morphological change of the NW after a time of ~100 ns.

As known, irradiation of composite materials by ultrafast laser pulses usually involves very large heating/cooling rates. With the incoming heating pulses, the top bead and the GaAs NW are

Table 1. Latent heat and specific heat for two alloy phases

Phase	Latent heat, kJ/mol	Specific heat, J/(mol·K)
Au_7Ga_2	8	62
AuGa	21	41

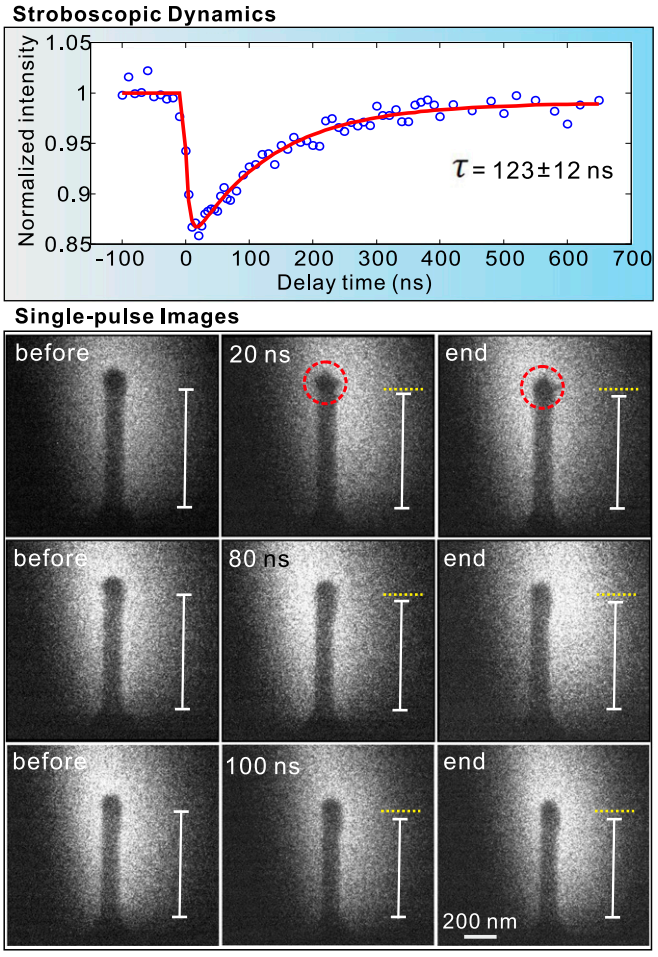

Fig. 4. Time-resolved dynamics of the NW. (*Upper*) Normalized diffraction intensity vs. delay time, indicating cooling dynamics with a time constant of 123 ± 12 ns. The fitting is shown in the red line. (*Lower*) Single-pulse images of the NW at a specific delay time. The images in *Lower Left*, *Center*, and *RIght* correspond to the states of the NW before, at specific delays, and after the process ended (the incident laser pulse has been removed), respectively. Three rows of images are associated with the NW states at the delay time of 20, 80, and 100 ns, respectively. Besides the length shrinkage, the transient shape changes of the top bead (marked with a circle) at different delays were also captured. The white rulers indicate the NW length. For easy comparison, the dotted yellow lines are the top reference lines in the initial states before laser pulse excitation (first column images). The electric field of the pump laser pulse was parallel to the long axis of the NW.

"hot," but remain solid until regions of melt phase nucleate. Under a large heating rate, it enables fast motion of the involved atoms of the melt phase near the interface (the temperature for melting at this region is much lower than the melting point of each individual component). The melt phase starts to nucleate at the Au/GaAs interface and to expand into the materials. Nevertheless, thermal diffusion near the interface limits the expansion of the melt region through cooling the photoexcited region. Therefore, after a short period of time, the temperature of the melt portion drops to the eutectic isotherm, and the alloy phases begin to nucleate and finally solidify to form the alloys.

For the scenario of a free-space diffusion process, we estimated the diffusion constant using $l = \sqrt{2D\tau}$, where l is the diffusion length, D is the diffusion coefficient, and τ is the time. From the single-pulse images in Fig. 4, the NW length showed a ~30-nm reduction at 20 ns (Fig. 4, *Lower*, center image in the first row) and continued a shrinkage of ~15 nm after the laser pulse (Fig. 4, *Lower*, first row, rightmost image). The corresponding diffusion

constant was estimated on an order of 10^{-4} cm^2/s, which was at least several orders of magnitude higher than the diffusivity of Au in GaAs and/or that of Ga in Au (28, 32–34). In comparison, the distance traveled by a ballistic gold or gallium atom with thermal velocity at the same temperature and time span would be on the order of micrometers, much larger than our observed NW length reduction. Therefore, the large reduction rate of the NW reported in this work suggests that the process cannot simply be diffusion-dominated processes, but, rather, indicates an important role due to the surface tension forces. Due to such surface-tension resultant forces, the reduction of 30 nm in NW length after a laser heating pulse could be fast—several orders of magnitude faster than the free-space diffusion or gravitational pull. The shape of the bead was maintained close to a sphere, even though its size grew with the number of laser heating pulses. Such spherical shape preservation is also an effect of surface tension; otherwise, the melt bead would drip down the GaAs NW, similar to melting wax tearing down from a burning candlestick. Furthermore, there was no obvious length change of the NW from 80 ns (Fig. 4, *Lower*, center image in the second row) to the end state (right image). Such observation provided an important clue about the time needed for eutectic-related phase reactions and solidification to complete. It indicated that the nucleation and growth of the melt phases were complete in ~80 ns, and after that, they began to solidify due to the cooling.

Polarization-Dependent Phenomena. The above experiments were conducted under the condition where the electric field (*E*-field) of the pump laser pulse was parallel to the long axis of the NW. We have also examined the effect of *E*-field polarization on NW dynamics. Fig. 5 shows polarization-dependent eutectic-related dynamics of individual NWs with the *E*-field of the laser pulse polarized either parallel or perpendicular to the NW axial direction (schematically illustrated in Fig. 5 *C*, *Inset*). For parallel polarization, the morphology of the top bead (marked by a circle) began to change at a laser fluence of 6.5 mJ/cm^2 (Fig. 5 *A*, *Left* and *Center*). The threshold laser fluence for the morphological change of the bead, however, increased to 8.2 mJ/cm^2 with a perpendicular polarization (Fig. 5 *B*, *Left* and *Center*). It indicated the enhancement of eutectic-related reactions at the Au/GaAs interface for the parallel *E*-field polarization. With an incoming single laser pulse above the threshold (fluence of 13 mJ/cm^2), the length reduction of the GaAs NW was ~76 nm for parallel *E*-field polarization, compared with that of a smaller reduction of ~48 nm for perpendicular polarization (Fig. 5 *A* and *B*, *Right*). Shown in Fig. 5*C* is the length reduction of the NW at a fluence of 13 mJ/cm^2 with a chain of laser shots (up to five). The NW length reduction became smaller with increasing the number of laser shots, and finally decreased to nearly zero on the fifth laser shot. The shrinkage of the NW length became increasingly difficult (only increasing the number of laser shots) at a fixed laser fluence due to the presence of latent heat of the newly formed alloys.

It is noteworthy that at each laser shot, the length reduction of the NW was always larger in parallel *E*-field polarization than that in the perpendicular one (Fig. 5*C*). This result elucidates that the observed reaction was dependent on the laser *E*-field polarization. Under laser pulse excitation, collective electron oscillations on a nanostructure by incident laser (electromagnetic field) gives rise to localized surface plasmons (strong charge densities of opposite sign at both sides of the nanostructure), whose field distribution is determined by the *E*-field polarization of the incident laser. Compared with perpendicular *E*-field polarization, the localized surface plasmon fields in the case of parallel polarization (electron oscillations are along the long axis of the nanostructure) would be enhanced near the bead/NW interfacial region (35–39), resulting in strong local photothermal effect at the interface where the eutectic-related reaction takes place. In addition, parallel *E*-field polarization leads to a further enhancement in optical absorption (causing higher temperature) along the NW (40, 41). Because of these enhancement effects, the laser fluence threshold for achieving the eutectic-related reactions reduces in the case of parallel field polarization, while at the same laser fluence, the length reduction of the NW (swallowed by the top nanoparticle due to eutectic-related reactions) is larger in the parallel polarization than that in the perpendicular one, as experimentally observed in Fig. 5.

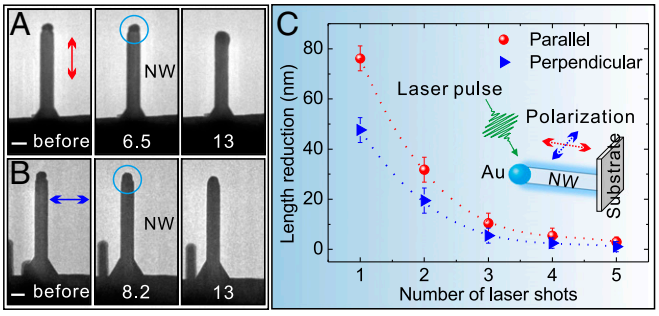

Fig. 5. Polarization-dependent dynamics. (*A*) Electron micrographs of a NW before and after a laser pulse whose *E*-field polarization is parallel to the long axis of the NW. (Scale bar, 100 nm.) (*B*) Electron micrographs of a NW before and after a laser pulse, but with a perpendicular *E*-field polarization. (Scale bar, 100 nm.) *A* and *B*, *Center* and *Right* correspond to the images at different laser fluences (unit is mJ/cm^2). The circles indicate the morphological change of the top bead. (*C*) Length reduction of the GaAs NWs at different polarization directions. For each polarization, the laser fluence is 13 mJ/cm^2. The length reduction was determined from the NW length change after each laser shot. (*C*, *Inset*) Schematic diagram showing a NW excited by a laser pulse with its *E*-field polarization parallel or perpendicular to the long axis of the NW.

Conclusions

In summary, our findings suggest that the eutectic-related phase reaction processes of the NWs can be controlled/designed via tailoring the fluence, polarization, and number of laser pulses in the pulse sequence, providing the potential of eutectic bonding/welding to a desired/targeted location in microdevices/nanodevices. The ability to fine-tune the nanoparticle size and shape is important for plasmonics applications (42–44). Additionally, using a simple design and nondestructive preparation technique of as-grown free-standing nanowires (without supporting films), we were able to effectively study the anisotropic (orientation-dependent) properties of the NWs in their native environment with better statistics. Using 4D single-pulse imaging of multiphase eutectic-related processes in nanostructured materials as an example, we clearly demonstrated the potential of this technique for exploring irreversible chemical/physical reaction dynamics at high spatial and temporal resolution so that the underlying mechanisms in complex systems could be unraveled. The powerful capabilities of 4D EM provide in situ manipulation and visualization of irreversible processes in space and time and therefore offer a valuable tool to investigate photochemical reactions as well as macromolecular dynamics in biological systems.

Materials and Methods

Preparation of Au/GaAs NWs. The gold-catalyzed GaAs NWs were epitaxially grown on a GaAs $(111)_B$-oriented substrate by metal–organic chemical vapor deposition. The catalysts used for the growth were gold nanoparticles. Initially, the GaAs substrate was treated with poly-L-lysine solution, followed by a solution of colloidal Au nanoparticles ~100 nm in diameter. The major role of catalyst Au was to lower the nucleation energy of each grown layer at the seed/substrate interface, promoting the growth of NWs. Before growth, the substrate was annealed at 600 °C under AsH_3 ambient to remove surface contaminants. The substrate was then cooled to 550 °C, and the NW growth proceeded by injecting the precursors of trimethylgallium and AsH_3 to the growth chamber with ultra-high-purity hydrogen as the carrier gas. Details of the growth procedures of GaAs NWs are available elsewhere (45, 46).

Sample Preparation for 4D Imaging. Normally, to prepare NW samples for TEM studies, the NWs grown on a substrate are transferred to a metal grid (200–2,000 mesh) or to a grid with supporting films (carbon, silicon monoxide, silicon nitride, etc.). During the transfer process, the NWs are either broken into several

segments (permanent damage), contaminated, or aggregated. In this work, we prepared the NW samples without any damage or using supporting films. First, the substrate containing free-standing GaAs NWs was cut into small pieces with dimensions of $\sim 2 \times 1 \times 0.3$ mm^3. One side of the small piece (the side of the 0.3-mm thickness) was glued on a common copper O-ring. Then, the copper O-ring with the sample was directly mounted on the TEM holder for investigation (*SI Appendix*, Fig. S1). This method of sample preparation excluded any disturbance from the supporting films normally present in TEM grids. Furthermore, this type of sample preparation allowed us to investigate the properties of a single NW with better statistics (because all NWs grown on the substrate have the similar orientation and direction, we could choose many of them to obtain the statistical data).

Spatiotemporal Visualization of Eutectic-Related Dynamics. The morphology of GaAs NWs was investigated by using an FEI scanning electron microscope. The studies of the eutectic-related dynamics and control of Au/GaAs NWs were conducted by 4D EM (Fig. 1*A*). The 4D EM was equipped with laser systems, which could operate in either stroboscopic (for reversible processes) or single-pulse mode (for irreversible dynamics). Both modes were used in this work. Picosecond green laser pulses at 532 nm (16-ps pulse duration) were used to heat the sample and to initiate the reactions, whereas nanosecond UV laser pulses at 266 nm (10-ns pulse duration) were directed to the photocathode to generate electron pulses. The photoelectrons in each pulse for probing were then accelerated to 120 keV, corresponding to a de Broglie wavelength of 3.3 pm. The timing between the pump pulse and the probe pulse was controlled by changing the delay time between the two through a digital delay generator.

The NW transient morphologies during the eutectic-related reactions were captured by single-pulse imaging mode of 4D EM, where an entire image was acquired with only one electron pulse (containing $\sim 10^5$ electrons), following an excitation laser pulse. For stroboscopic experiments, the repetition rate was set at 1 kHz, ensuring the full recovery of the dynamical process. Details of the procedure are given in previous studies from this group (47–49). Selected-area electron diffraction was performed to identify the structures of the NWs and the newly formed alloy phases. Three kinds of modes were used—namely, TEM, stroboscopic (1 kHz), and single-pulse modes.

Polarization-Dependent Behavior. We used a femtosecond laser (wavelength of 520 nm, pulse duration of 350 fs) to excite the NW dynamics and probed the eutectic-related behavior of the NWs with an electron beam. A polarizer was used to set the *E*-field polarization of the laser pulse either parallel or perpendicular to the long axis of the NWs (schematic diagram in Fig. 5). For each polarization direction, a single laser pulse irradiated the NW sample at each time. The subsequent morphological change and length reduction of the NWs, which were due to the reaction between the Au and GaAs, were directly visualized by the electron beam.

ACKNOWLEDGMENTS. We thank J. S. Baskin and J. S. Huang for very helpful discussion. This work was supported by Air Force Office of Scientific Research Grant FA9550-11-1-0055S in the Gordon and Betty Moore Foundation for Physical Biology Center for Ultrafast Science and Technology at California Institute of Technology. M.L., H.H.T., and C.J. thank the Australian Research Council for support and the Australian National Fabrication Facility for access to the epitaxial facilities used in this work.

1. Nadella R, Eskin DG, Du Q, Katgerman L (2008) Macrosegration in direct-chill casting of aluminium alloys. *Prog Mater Sci* 53:421–480.
2. Woodall JM (1980) III-V compounds and alloys: An update. *Science* 208:908–915.
3. del Alamo JA (2011) Nanometre-scale electronics with III-V compound semiconductors. *Nature* 479:317–323.
4. Wolffenbuttel RF, Wise KD (1994) Low-temperature silicon wafer-to-wafer bonding using gold at eutectic temperature. *Sens Actuators A Phys* 43:223–229.
5. Kim BJ, et al. (2008) Kinetics of individual nucleation events observed in nanoscale vapor-liquid-solid growth. *Science* 322:1070–1073.
6. Schülli TU, et al. (2010) Substrate-enhanced supercooling in AuSi eutectic droplets. *Nature* 464:1174–1177.
7. Shpyrko OG, et al. (2006) Surface crystallization in a liquid AuSi alloy. *Science* 313: 77–80.
8. LLorca J, Orera VM (2006) Directionally solidified eutectic ceramic oxides. *Prog Mater Sci* 51:711–809.
9. De Rosa, Park C, Thomas EL, Lotz B (2000) Microdomain patterns from directional eutectic solidification and epitaxy. *Nature* 405:433–437.
10. Kodambaka S, Tersoff J, Reuter MC, Ross FM (2007) Germanium nanowire growth below the eutectic temperature. *Science* 316:729–732.
11. Holmberg VC, Panthani MG, Korgel BA (2009) Phase transitions, melting dynamics, and solid-state diffusion in a nano test tube. *Science* 326:405–407.
12. Shahani AJ, Xiao X, Voorhees PW (2016) The mechanism of eutectic growth in highly anisotropic materials. *Nat Commun* 7:12953.
13. Mckeown JT, et al. (2016) Time-resolved in situ measurements during rapid alloy solidification: Experimental insight for additive manufacturing. *JOM* 68:985–999.
14. Barwick B, Flannigan DJ, Zewail AH (2009) Photon-induced near-field electron microscopy. *Nature* 462:902–906.
15. Carbone F, Kwon OH, Zewail AH (2009) Dynamics of chemical bonding mapped by energy-resolved 4D electron microscopy. *Science* 325:181–184.
16. Kwon OH, Ortalan V, Zewail AH (2011) Macromolecular structural dynamics visualized by pulsed dose control in 4D electron microscopy. *Proc Natl Acad Sci USA* 108: 6026–6031.
17. Yurtsever A, Zewail AH (2011) Kikuchi ultrafast nanodiffraction in four-dimensional electron microscopy. *Proc Natl Acad Sci USA* 108:3152–3156.
18. van der Veen RM, Kwon OH, Tissot A, Hauser A, Zewail AH (2013) Single-nanoparticle phase transitions visualized by four-dimensional electron microscopy. *Nat Chem* 5: 395–402.
19. Fu X, Chen B, Tang J, Hassan MT, Zewail AH (2017) Imaging rotational dynamics of nanoparticles in liquid by 4D electron microscopy. *Science* 355:494–498.
20. Joyce HJ, et al. (2011) III-V semiconductor nanowires for optoelectronic device applications. *Prog Quantum Electron* 35:23–75.
21. Chen B, et al. (2013) Strengthening brittle semiconductor nanowires through stacking faults: Insights from in situ mechanical testing. *Nano Lett* 13:4369–4373.
22. Wang J, Liu YJ, Liu LB, Zhou HY, Jin ZP (2011) Thermodynamic assessment of the Au-Ga binary system. *Calphad* 35:242–248.
23. Panish MB (1967) Ternary condensed phase systems of gallium and arsenic with group IB elements. *J Electrochem Soc* 114:516–521.
24. Duan XF, Lieber CM (2000) General synthesis of compound semiconductor nanowires. *Adv Mater* 12:298–302.
25. Stanchina WE, Whelan M (1983) Solubility of GaAs in Au-Ge eutectic melts. *Solid-State Electron* 26:817–819.
26. Mueller CH, Holloway PH, Connell RG (1992) The ternary phase diagram for Au-Ga-As using flow chart technique. *MRS Proc* 260:481.
27. Schmid-Fetzer R (1994) *Ternary Alloys—A Comprehensive Compendium of Evaluated Constitutional Data and Phase Diagrams*, eds Petzow G, Effenberg G, Aldinger F (VCH, Weinheim, Germany), Vol 9.
28. Persson AI, et al. (2004) Solid-phase diffusion mechanism for GaAs nanowire growth. *Nat Mater* 3:677–681.
29. Blakemore JS (1982) Semiconducting and other major properties of gallium arsenide. *J Appl Phys* 53:R123–R181.
30. Kuanr AV, Bansal SK, Srivastava GP (1996) Laser induced damage in GaAs at 1.06 μm wavelength: Surface effects. *Opt Laser Technol* 28:25–34.
31. McGilp JF (1987) Alloying and entropy effects in predicting metal/compound semiconductor interface reactivity. *J Mater Res* 2:516–523.
32. Patuwathavithane CS, Williams JR, Tin CC, Barnes PA, Bozack MJ (1991) An RBS analysis of the low temperature mass transport of Au in GaAs. *Nucl Instrum Methods Phys Res B* 56–57:753–756.
33. Fisher DJ (1998) *Diffusion in GaAs and Other III-V Semiconductors: 10 Years of Research* (Trans Tech Publications, Zurich).
34. Gupta RP, Khokle WS, Wuerfl J, Hartnagel HL (1987) Diffusion of gallium in thin gold films on GaAs. *Thin Solid Films* 151:L121–L125.
35. Barrow SJ, Wei X, Baldauf JS, Funston AM, Mulvaney P (2012) The surface plasmon modes of self-assembled gold nanocrystals. *Nat Commun* 3:1275.
36. Miyanishi T, Terakawa M, Obara M, Nedyalkov NN, Atanasov PA (2010) Directionally-controlled plasmon excitation in gold nanoparticles for near-field nanopatterning by femtosecond laser. *Proc SPIE* 7751:77511X.
37. Brongersma ML, Halas NJ, Nordlander P (2015) Plasmon-induced hot carrier science and technology. *Nat Nanotechnol* 10:25–34.
38. Atwater HA, Polman A (2010) Plasmonics for improved photovoltaic devices. *Nat Mater* 9:205–213.
39. Li Y, Yan X, Wu Y, Zhang X, Ren X (2015) Plasmon-enhanced light absorption in GaAs nanowire array solar cells. *Nanoscale Res Lett* 10:436.
40. Gu ZQ, Prete P, Lovergine N, Nabet B (2011) On optical properties of GaAs and GaAs/AlGaAs core-shell periodic nanowire arrays. *J Appl Phys* 109:064314.
41. Wang B, Stevens E, Leu PW (2014) Strong broadband absorption in GaAs nanocone and nanowire arrays for solar cells. *Opt Express* 22:A386–A395.
42. Jin R, et al. (2001) Photoinduced conversion of silver nanospheres to nanoprisms. *Science* 294:1901–1903.
43. Jain PK, Huang X, El-Sayed IH, El-Sayed MA (2008) Noble metals on the nanoscale: Optical and photothermal properties and some applications in imaging, sensing, biology, and medicine. *Acc Chem Res* 41:1578–1586.
44. Byers CP, et al. (2015) From tunable core-shell nanoparticles to plasmonic drawbridges: Active control of nanoparticle optical properties. *Sci Adv* 1:e1500988.
45. Joyce HJ, et al. (2007) Twin-free uniform epitaxial GaAs nanowires grown by a two-temperature process. *Nano Lett* 7:921–926.
46. Joyce HJ, Wong-Leung J, Gao Q, Tan HH, Jagadish C (2010) Phase perfection in zinc blende and wurtzite III-V nanowires using basic growth parameters. *Nano Lett* 10: 908–915.
47. Flannigan DJ, Samartzis PC, Yurtsever A, Zewail AH (2009) Nanomechanical motions of cantilevers: Direct imaging in real space and time with 4D electron microscopy. *Nano Lett* 9:875–881.
48. Park ST, Flannigan DJ, Zewail AH (2011) Irreversible chemical reactions visualized in space and time with 4D electron microscopy. *J Am Chem Soc* 133:1730–1733.
49. Lorenz UJ, Zewail AH (2014) Nanofluidics. Observing liquid flow in nanotubes by 4D electron microscopy. *Science* 344:1496–1500.